Molecular imaging of plant-microbe interactions on the Brachypodium seed surface

Journal:	*Analyst*
Manuscript ID	AN-ART-02-2021-000205.R1
Article Type:	Paper
Date Submitted by the Author:	08-Jul-2021
Complete List of Authors:	Zhang, Yuchen; Pacific Northwest National Laboratory , Energy and Environment Directorate Komorek, Rachel; Pacific Northwest National Laboratory , Earth and Enviornment Directorate Son, Jiyoung; Pacific Northwest National Laboratory Riechers, Shawn ; Pacific Northwest National Laboratory, Energy and Environment Directorate Zhu, Zihua; Pacific Northwest National Laboratory , Environmental Molecular Sciences Laboratory Jansson, Janet; Pacific Nortwest National Laboratory Jansson, Christer; Pacific Northwest National laboratory, Environmental Molecular Sciences Laboratory Yu, Xiao-Ying; Pacific Northwest National Laboratory, Energy and Environment Directorate

1
2
3
4

Analyst

5
6
7

PAPER

8
9
10
11

Molecular imaging of plant-microbe interactions on the *Brachypodium* seed surface

12
13

Yuchen Zhang[a], Rachel Komorek[a], Jiyoung Son[a], Shawn Riechers[a], Zihua Zhu[b], Janet Jansson[c], Christer Jansson[b] and Xiao-Ying Yu*[a]

Plant growth-promoting rhizobacteria (PGPR) play a crucial role in biological control and pathogenic defense on and within plant tissues, however the mechanism(s) by which plants associate with PGPR to elicit such beneficial effects needs further study. Here, we present time-of-flight secondary ion mass spectrometry (ToF-SIMS) imaging of *Brachypodium distachyon* (Brachypodium) seeds with and without exposure to two model PGPR, i.e., Gram-negative *Pseudomonas fluorescens SBW25* (*P.*) and Gram-positive *Arthrobacter chlorophenolicus* A6 (*A.*). Delayed image extraction was used to image PGPR-treated seed sections to reveal morphological changes. ToF-SIMS spectral comparison, principal component analysis (PCA), and two-dimensional (2D) imaging show that the selected PGPR have different effects on the host seed surface, resulting in changes in chemical composition and morphology. Metabolite products and biomarkers, such as flavonoids, phenolic compounds, fatty acids, and indole-3-acetic acid (IAA), were identified on the PGPR-treated seed surfaces. These compounds have different distributions on the Brachypodium seed surface for the two PGPR, indicating that the different bacteria elicite distinct responses from the host. Our results illustrate that ToF-SIMS is an effective tool to study plant-microbe interactions and to provide insightful information with submicrometer lateral resolution of the chemical distributions associated with morphological features, potentially offering a new way to study the mechanisms underlying beneficial roles of PGPR.

Introduction

Plant growth-promoting rhizo bacteria (PGPR) are known to support plant growth and fitness [1,2] and their utilization in agricultural practice is an attractive strategy for sustainable enhancement of crop productivity.[3] Accordingly, investigations of the mechanisms underlying the beneficial properties of PGPR for plant growth promotion are needed. PGPR are known to affect plant growth by moderating plant hormone indole acetic acid (IAA). IAA is a common plant-derived auxin and can also be synthesized by some PGPR, including some pseudomonads.[4-6] However, details of the metabolic interactions that occur between plants and specific PGPR at the microscopic scale are still lacking.[7]

Several new molecular-scale imaging platforms show promise for high resolution characterization of specific metabolic and spatial interactions between PGPR and plant surfaces. Mass spectrometric imaging, including desorption electrospray ionization mass spectrometry (DESI-MS), laser ablation electrospray ionization mass spectrometry (LAESI-MS), matrix-assisted laser desorption ionization mass spectrometry

(MALDI-MS), and secondary ion mass spectrometry (SIMS) [8], provide molecular-level imaging and information on chemical spatial distributions on the surface of plant samples.[9,10] DESI and LAESI are ambient ionization techniques, in which samples are analyzed under ambient pressure with supermicrometer lateral resolution. DESI-MS has been used to detect molecular signatures on leaf and flower surfaces.[11] LAESI has been combined with ion mobility separation (IMS) to distinguish structurally dissimilar isomers and conformers in leaves. MALDI can detect larger ions, such as peptides and proteins; and it has been used to analyze the distribution of metabolites, such as amino acids, sugars and phosphorylated metabolites on the plant surface.[12] MALDI and other omics approaches have also been used to study protein-mediated lignan and cyanogenic glucoside formation in plants.[13]

Compared to MALDI-MS, time-of-flight secondary ion mass spectrometry (ToF-SIMS) does not depend on the matrix application to enable detection.[14] Meanwhile, the lateral resolution of ToF-SIMS is about ~0.2 μm, offering much higher spatial resolution than MALDI-MS, DESI-MS, or LASEI-MS.[15] Thus, single-cell metabolomics is possible with ToF-SIMS, because it offers submicrometer spatial resolution.[16] For example, flavonoids have been mapped using ToF-SIMS in peas and *Arabidopsis thaliana.*[17] The spatial resolution in MALDI-MS is generally in the range of several micrometers and in DESI-MS and LAESI-MS tens to hundreds micrometers.[18,19] We recently applied correlative imaging of Brachypodium and *Pseudomonas fluorescens* SBW25 to showcase the use of ToF-SIMS.[20]

a. *Energy and Environment Directorate, Pacific Northwest National Laboratory, Richland, WA 99354, USA, E-mail: xiaoying.yu@pnnl.gov*
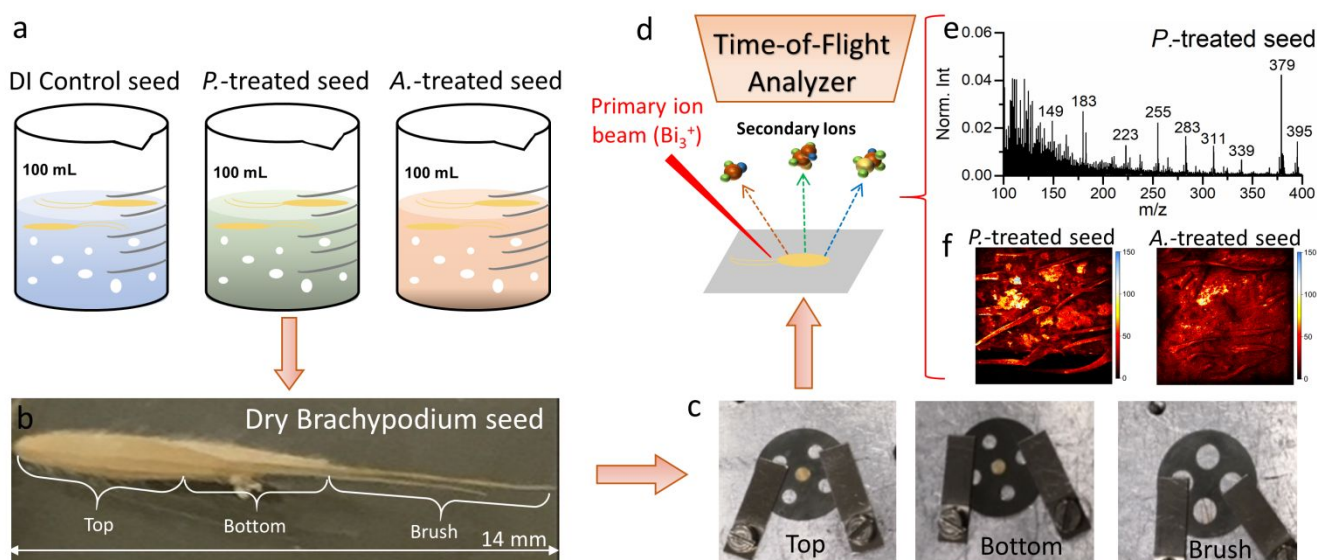b. *Environmental and Molecular Science Laboratory, Pacific Northwest National Laboratory, Richland, WA 99354, USA*
c. *Earth and Biological Science Directorate, Pacific Northwest National Laboratory, Richland, WA 99354, USA*

Analyst

PAPER

Fig. 1. Schematics of seed sample preparation. (a) Brachypodium seeds were divided into three segments: top, bottom and brush. Three treatments were performed on Brachypodium seeds including DI water control, P.- and A.-treated seed. Prior to ToF-SIMS analysis, PGPR-treated Brachypodium seeds were cut into three segments (b), then secured in sample holders (c) and placed in the ToF-SIMS main stage (d). (e) A representative ToF-SIMS negative spectrum of the P.-treated seed in m/z− 100-400 and (f) representative ToF-SIMS negative 2D total ion images of PGPR-treated seeds.

Brachypodium is an important model for grasses, including bioenergy crops and cereals.[1] We aimed to elucidate specific plant-microbe interactions by utilizing the multimodal imaging capability of ToF-SIMS in this work. ToF-SIMS is useful to obtain more information on plant surface metabolic interactions between PGPR and the host plant.

Although ToF-SIMS is perceived as a powerful imaging technique, its application in plant biology is not as popular compared to MALDI.[21] The interactions of a model biofuel feedstock, Brachypodium, with two types of PGPR, Gram-negative *Pseudomonas fluorescens SW25* (*P.*) and Gram-positive *Arthrobacter chlorophenolicus* A6 (*A.*), [22, 23] were chemically imaged using ToF-SIMS in this work. Moreover, delayed image extraction mode was used to improve the mass resolution while preserving the spatial resolution during imaging, [24, 25] allowing for enhanced mass resolution by extracting secondary ions from the sample surface with a specific time delay after the arrival of primary ions.[26] The delayed image extraction mode has been applied in MALDI and ToF-SIMS imaging as a promising strategy.[27-29] We hypothesized that the Gram-positive *A.* and Gram-negative *P.* would exert distinct effects on the seed surface of the Brachypodium plant host. Second, we postulated that responses in the host should vary along seed sections due to the difference in growth potential. Our findings provide valuable

biological insights into metabolites and biomarkers in plant-PGPR interactions and give more confidence in using the multimodal imaging capability of ToF-SIMS in future studies of plant and microbial sciences.

Experimental

PGPR preparation

The green fluorescent protein-tagged *Pseudomonas fluorescens* SBW25 and *Arthrobacter chlorophenolicus* A6 strains were obtained from previous studies.[22, 23] The bacteria were cultured on Luria Broth (LB) agar plates at 30 ℃ 24 h, until individual colonies appeared. Both strains are kanamycin resistant. Therefore, the two strains were individually grown in 20 mL LB and kanamycin (50 µg/mL) medium in 50 mL serum bottles with shaking at 150 rpm at 30 ℃. A bubble trap was prepared to analyze the liquid vacuum interface (SALVI) in a microfluidic microchannel as described previously.[30-32] A 10 mL syringe was filled with 9 mL of the LB and kanamycin medium that was connected to a polyetheretherketon (PEEK) that fit onto the microfluidic system. A syringe pump was set to run for 20 µL /min to let the medium flow across the microchannel for 12 h. After the bacteria in the serum bottles grew to log phase (~ 24 h), the cultures were inoculated at the liquid vacuum interface

(SALVI) microchannel and the flow rate was set to 2 μL /min for biofilm culturing.[33] After 5 – 6 days, visible biofilm growth was observed in the microchannel. The biofilm growth setup is illustrated in Fig. S1.

For preparation of planktonic bacterial cells, strains *P.* and *A.* were inoculated into 50 mL flasks containing 5 mL LB medium and cultured 1 – 2 days at 30 ℃ until the cultures reached an optical density (OD_{600}) of approximately 0.6. Subsequently, planktonic cells were harvested by centrifugation (5430, Eppendorf) for 2 min at 734 g. The supernatant was discarded

and 1 mL of sterile, deionized (DI) water was added to resuspend the precipitated bacteria before centrifuging one more time. This step was repeated three times for desalination. Finally, 20 μL of the suspension was extracted with a pipette after discarding the supernatant and resuspending the bacteria in 200 μL of sterile DI water.

All samples were dried by air under a laminar flow in a fume hood and then deposited on a clean silicon (Si) wafer (10 mm × 10 mm diced, Ted Pella Inc) before ToF-SIMS analysis.[34]
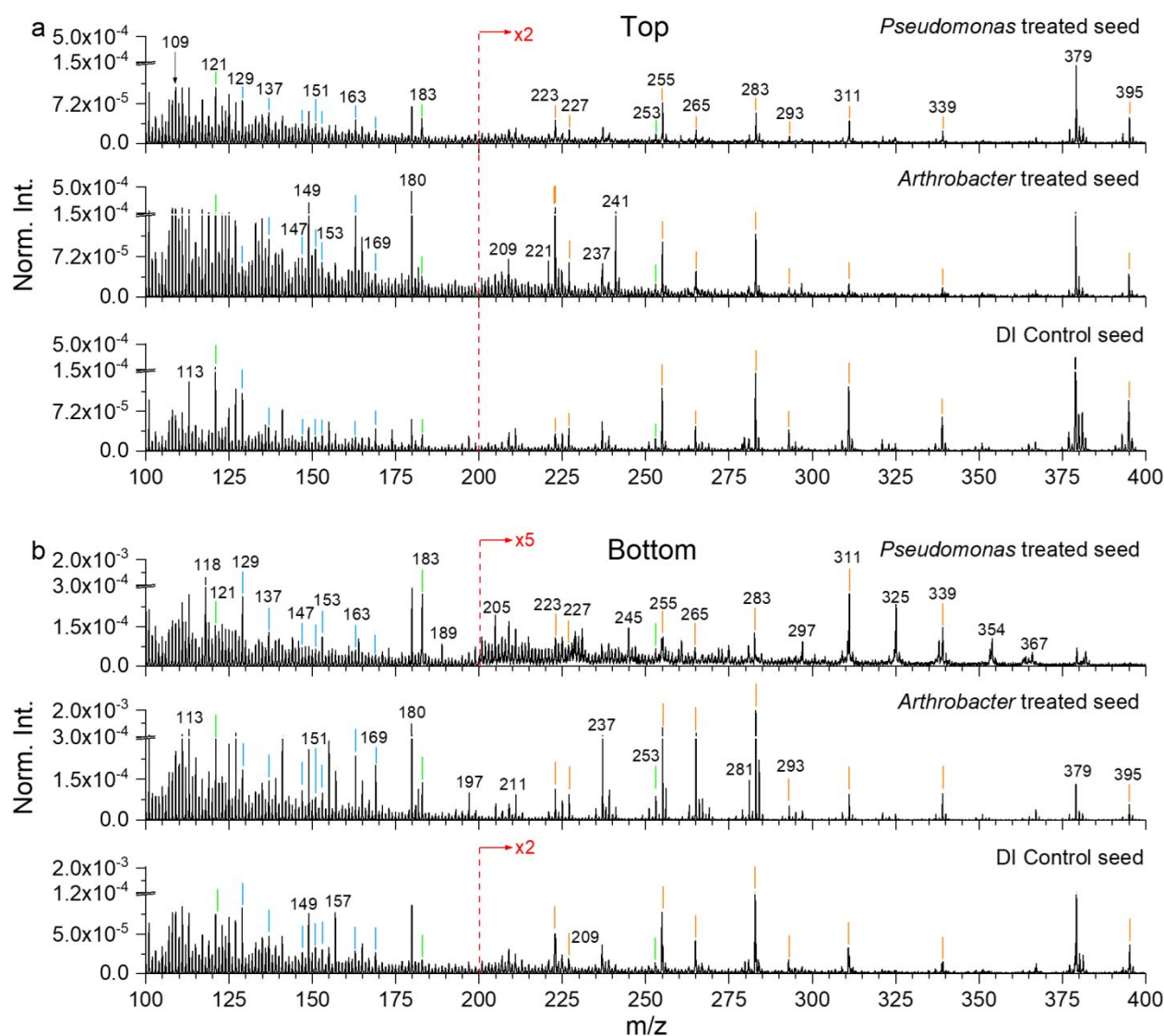
Fig. 2. Normalized spectral comparison plots among different treatments in (a) top of seed and (b) bottom of seed in the negative mode in the range of m/z^- 100 – 400. The green, blue, orange bars represent flavonoids fragments, phenolic acids and their derivatives, and fatty acids, respectively.

Brachypodium seed sample preparation

Brachypodium seeds (psb00001, Riken BRC Experimental Plant Division) were washed with sterile, deionized (DI) water in a 100 mL beaker for 24 h. These were used as control seeds. Similarly, *P.*-treated seeds were soaked in sterile DI water, followed by inoculation with a 400 μL aliquot of *P.* bacteria in a 40 mL LB medium solution. A third set of samples was prepared by inoculating the soaked seeds in the DI water with *A.* bacteria

(Fig. 1a). All beakers were sealed with Parafilm® and placed at 25 ℃ with no direct sunlight for 24 h under sterile conditions. Prior to ToF-SIMS analysis, the seeds were dried using nitrogen gas and cut into three segments (Fig. 1b), then secured in a sample holder (Fig. 1c). After ToF-SIMS analysis (Fig. 1d), SIMS spectra (Fig. 1e) and 2D (Fig. 1f) images were collected under the spectral mode and delayed image extraction mode, respectively.

ToF-SIMS analysis

We used an IONTOF ToF-SIMS V spectrometer (IONTOF GmbH, Münster, Germany). The primary ion was a 25 keV Bi_3^+ cluster ion beam in the spectral mode. The beam was focused in 5 μm diameter with a current of 0.56 pA at 10 kHz frequency. The main chamber pressure was maintained at ~8×10^{-9} mbar during analysis. ToF-SIMS spectra were acquired by scanning an area of 200 × 200 μm^2 in the top and bottom segments of seeds and an area of 100 × 100 μm^2 in the brush segment of seeds, respectively, for 100 scans with a pixel resolution of 128 × 128.

ToF-SIMS imaging with better spatial resolution was highly desirable using the delayed extraction imaging mode. The Bi_3^+ cluster ion beam was focused around 400 nm diameter with a current of 0.36 pA (150 ns pulse width) at 10 kHz frequency. The pressure of the main chamber was maintained at ~2.5×10^{-8} mbar. ToF-SIMS delayed extraction images were acquired by scanning an area of 500 × 500 μm^2 in the top and bottom segments of seeds and an area of 150 × 150 μm^2 in the brush segment of seeds, respectively, for 50 scans with a pixel resolution of 256 × 256. Mass resolution was between 2000 – 4000. Tables S2 gives examples of the mass resolution of selected peaks using the delayed extraction mode.

ToF-SIMS data were analyzed using the IONTOF Surface Lab 6.3 software. At least five positive and negative data points were collected for each sample. Mass spectra were calibrated using CH_2^+ (m/z^+ 14), $C_2H_3^+$ (m/z^+ 27), $C_{10}H_8O_3^+$ (m/z^+ 176), $C_{16}H_8^+$ (m/z^+ 200) and $C_{23}H_{21}$ (m/z^+ 297) peaks in the positive mode; and O^- (m/z^- 16), O_2H^- (m/z^- 33), $C_{11}H_{16}O^-$ (m/z^- 164), $C_{17}H_{21}O^-$ (m/z^- 241) and $C_{20}H_{29}O_4^-$ (m/z^- 333) peaks in the negative mode. Calibrated SIMS data were exported to Origin Pro (2019b) for plotting. Peaks from ToF-SIMS analysis were likely identified mainly according to previous mass spectrometry studies[35-37] and high mass-resolution results of ToF-SIMS.[31, 32, 34] Some plant metabolites were identified based on earlier liquid chromatography-tandem mass spectrometry (LC-MS) studies.[38-41] SIMS spectral results of the DI control seed are illustrated in Figs. S2-S5, showing good reproducibility and measurement precision.

Spectral PCA was performed using unit mass in Matlab (R2018b).[42] In the first round of PCA, all peaks in both negative and positive mode were included, and the results showed a prominent matrix effect. Interference mainly came from high mass inorganic peaks in the lower mass range of $m/z \leq 100$. Since we were most interested in peaks in the range of $m/z \geq 100$, the second round of PCA was conducted using selected peaks ranging from m/z 100 – 400. Prior to performing spectral PCA, data were pretreated by mean centering, normalization to the total ion intensity of selected peaks, and square root transformation.[32, 34, 43, 44]

Results and Discussion

Seed metabolites as a function of interactions with PGPR

Comparisons between the top and bottom segments of seeds from different treatments in the high mass-resolution spectral analysis in the negative mode are depicted in Fig. 2. Normalized spectral comparisons in both negative and positive mode in the mass range from m/z 0 – 400 are displayed in Figs. S6 and S7. Analyses of *A.* and *P.* planktonic cells and biofilms were performed as bacterial control samples. Figures S8-S11 give SIMS spectral comparisons among bacterial controls, non-treated dry seed, DI control seed, and PGPR-treated seed. Looking into the negative mode in the range of m/z^- 100 – 400 spectra in Fig. 2, a series of characteristic peaks related to metabolites indicative of plant activities are observed in the DI control seed and PGPR-treated seeds in both top and bottom segments.

Flavonoids and phenolic acids are significant secondary metabolites in plants.[45, 46] We observed the fragment of quercetin$[^{1, 2}B]^-$ (m/z^- 120.99, $C_7H_5O_2^-$), fragments of galangin (m/z^- 183.05, $C_{12}H_7O_2^-$), and dihydroxyflavone (m/z^- 252.96, $C_{15}H_{11}O_4^-$) in the negative mode SIMS spectra among all samples. Intensities of the quercetin and galangin fragments in the top and bottom segments are higher in the PGPR-treated seeds than in the DI control seed. Phenolic acids and their derivatives are detected in the mass range of < m/z^- 200. For example, p-hydroxybenzoic acid (m/z^- 137.02, $C_7H_5O_3^-$), cinnamic acid (m/z^- 147.04, $C_9H_7O_2^-$), vanillin (m/z^- 151.00, $C_8H_7O_3^-$), protocatechuic acid (m/z^- 153.02, $C_7H_5O_4^-$), p-coumaric acid (m/z^- 163.05, $C_6H_{11}O_5^-$), and gallic acid (m/z^- 169.02, $C_7H_5O_5^-$) are observed in the top and bottom segments. Overall, peaks of these compounds show higher intensities in the PGPR-treated seeds, especially in A.-treated seed compared to the DI control seed. These metabolites were commonly detected by previous LC-MS studies.[39-41, 47] Recently, other mass spectrometry techniques were used to study flavonoids and phenolic acids.[17, 37, 48, 49] We used ToF-SIMS to discover and determine the spatial locations of the metabolites in PGPR-treated seeds in this work.

ToF-SIMS was used in imaging fatty acids.[36, 50] Several fatty acid peaks are likely identified in the range of m/z^- 200 – 400. Myristic acid (m/z^- 222.98, $C_{14}H_{23}O_2^-$), palmitic acid (m/z^- 255.13, $C_{16}H_{31}O_2^-$), stearic acid (m/z^- 283.29, $C_{18}H_{35}O_2^-$), arachidic acid (m/z^- 311.32, $C_{20}H_{39}O_2^-$), heneicosanoic acid (m/z^- 325.11, $C_{21}H_{41}O_2^-$), docosanoic acid (m/z^- 339.36, $C_{22}H_{43}O_2^-$), and cerotic acid (m/z^- 395.33, $C_{26}H_{51}O_2^-$) are found in the top or bottom seed segments based on peak-identification criteria described in the experimental section. Myristic acid, palmitic acid, and stearic acid are abundant in the DI control seed and PGPR-treated seeds. Cerotic acid is not observed in the bottom of the *P.*-treated seed. Other fatty acids are also detected in the negative mode, such as margaric acid (m/z^- 265.28, $C_{17}H_{29}O_2^-$). Detailed possible peak identification is summarized in Tables S2 and S3. The presence of fatty acids with 8 to 24 carbon chain-length structures at the seed surface are expected, because they are found in the lipid phosphatidylcholine (PC) for storage in the membrane.[51]

Analyst

PAPER
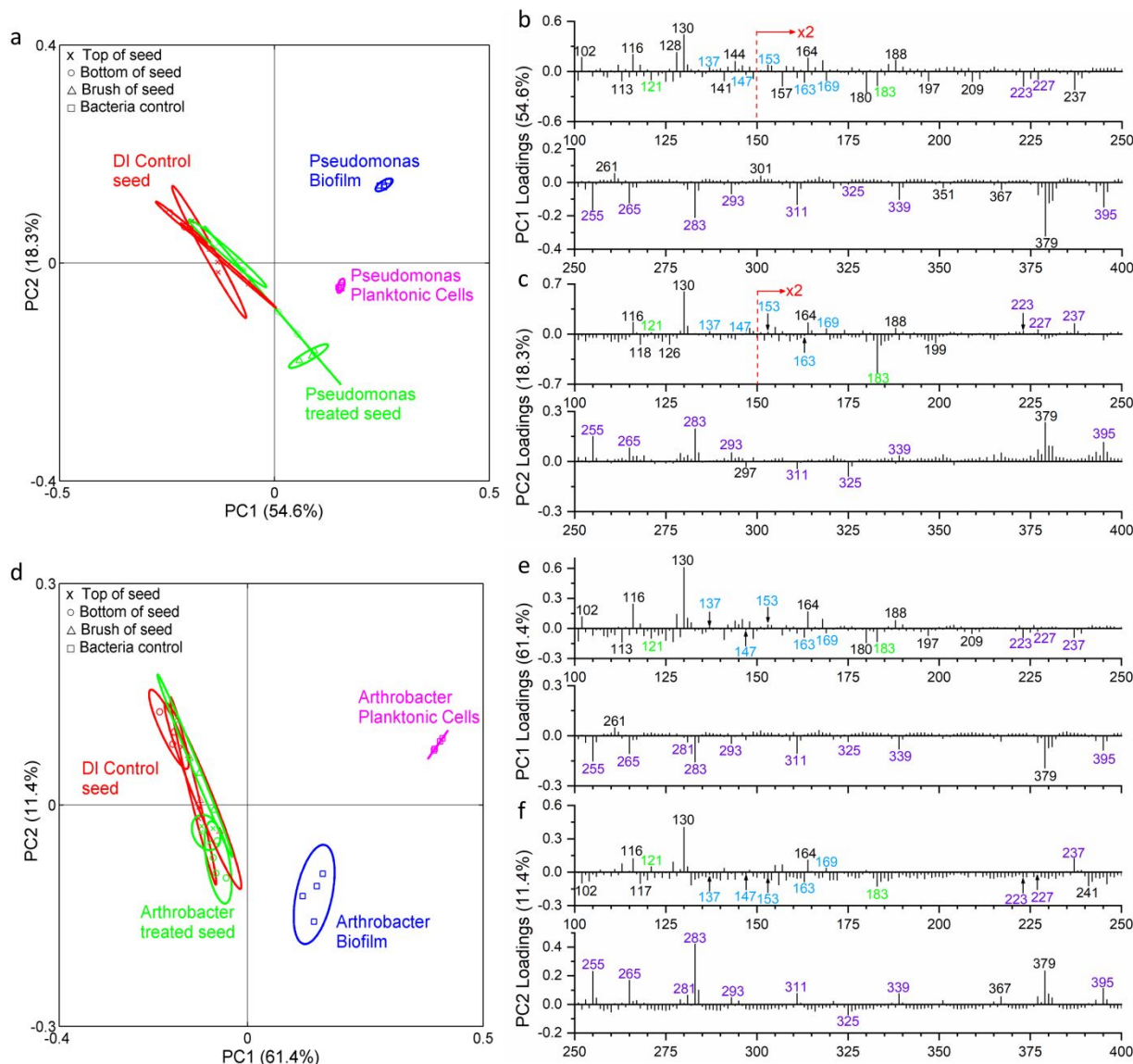
Fig. 3 Selected peak spectral PCA results in the negative ion mode: (a) PC1 vs. PC2 scores plot, (b) PC1 loadings plot, (c) PC2 loadings plot of the P.-treated samples, (d) PC1 vs. PC2 scores plot, (e) PC1 loadings plot, and (f) PC2 loadings in A.-treated samples. Peaks are labelled with their center masses. Peaks colored in green, blue, and purple represent flavonoids fragments, phenolic acids, and fatty acids, respectively.

Figure S7 depicts SIMS spectral comparison among the DI control seed and PGPR-treated seeds in the positive ion mode. Fatty acids, such as palmitic acid (m/z^+ 257.15, $C_{16}H_{33}O_2^+$), stearic acid (m/z^+ 285.17, $C_{18}H_{37}O_2^+$), arachidic acid (m/z^+ 313.21, $C_{20}H_{41}O_2^+$), and docosanoic acid (m/z^+ 341.37, $C_{22}H_{45}O_2^+$), are prominently found in both top and bottom segments of seeds. Furthermore, the intensities of peaks related to palmitic acid (m/z^+ 257.15, $C_{16}H_{33}O_2^+$), stearic acid (m/z^+ 285.17, $C_{18}H_{37}O_2^+$), and docosanoic acid (m/z^+ 341.37,

$C_{22}H_{45}O_2^+$) decrease remarkably in the bottom section of the *P.*-treated seed compared to the *A.*-treated and DI control seeds. Table S4 provides additional reference spectral information to support peak assignment.

Phospholipids are another class of lipids important for plant membranes and interactions with bacteria. Although phosphatidylethanolamine (PE) or PC fragments were not observed, m/z^+ 165.07 $C_{10}H_{13}O_2^+$ was potentially identified as an α-tocopherol fragment [52, 53] in all seeds in the positive mode

Paper

(Figs. S7a-b). α-tocopherol is a type of vitamin E located in the plastid or thylakoid membranes in plants, and the increase of α-tocopherol contributes to plant stress tolerance.[54] It functions to shield lipids and other membrane structures.[55] The intensity of α-tocopherol fragment reduces from the top to bottom segments in our SIMS spectral results, suggesting that the bottom of the seed exhibits higher response after being exposed to PGPR. A previous study summarizes the direct or indirect plant growth-promoting function of vitamins produced by PGPR, such as thiamin, niacin, and pyrroloquinoline quinine.[56] Our result indicates the potential role of vitamin E in the PGPR-plant interaction.

The peak of m/z^+ 174.96 observed in the positive mode in Figs. S7a-b is likely identified as IAA ($C_{10}H_9NO_2^+$).[57] IAA is the most naturally occurring auxin and a plant growth-promoting hormone. IAA is also produced as a signaling molecule in plants [58] and several rhizobacteria.[59] Specific strains of *Pseudomonas* and *Arthrobacter* were reported to produce IAA.[60-64] IAA is observed at the top of *P.*-treated seed in our spectral data, suggesting that IAA exists in the Gram-negative *P.* to enhance host plant growth. We will explore IAA's other functions in the following PCA discussion.

Spectral PCA showing interactions between PGPRs and the host seed surface

Spectral comparison alone cannot distinguish the contribution, response, and source of metabolites, fatty acids, and quorum sensing biomarkers, and determine whether they originate from the microbes or the plant. Therefore, spectral PCA is necessary for further evaluation of ToF-SIMS data. We break the data into two subsets to study the effects of the Gram-positive and Gram-negative PGPR individually in the following, *P.*-treated seed, DI control seed, *P.*-bacteria controls, and *A.*-treated seed, DI control seed and *A.*-bacteria controls in selected peak PCA. All peak spectral PCA scores and loadings plots in the positive mode are presented in Figs. S12 and S13 for comparison. We will focus on the results from selected peak spectral PCA because spectral overlay helps reduce the matrix effect.[65]

Figure 3a shows the spectral PCA scores plots of principal component 1 (PC1) vs. PC2 of *P.*-treated samples in the negative ion mode. PC1, PC2, and PC3 explain 54.6%, 18.3 %, and 8.9% of all data. PC1 separates the samples with and without seed; PC2 separates those with Pseudomonas from the others. These samples are well separated because of the difference of their surfaces. Strong topographical features at the seed surface and factors like bacterial treatment are contributors to this clustering.

The PC2 and PC4 scores and loadings plots are presented in Fig. S14. PC1 mainly separates the DI control seed as well as top and bottom segments of the *P.*-treated seeds from the *P.* bacteria control and the brush section of the *P.*-treated seed. PC2 positive shows overlaps between the *P.* biofilm and the upper segments of the *P.*-treated seed. Whereas PC2 negative has similarities among *P.* planktonic cells and the brush of the *P.*-treated seed. The scores plots of PC1 vs. PC2 and PC2 vs. PC4 indicate that both *P.* biofilms and planktonic cells affect the

seed surface. Moreover, the brush segment of the seed has more active *P.* bacteria cell interactions than the top and bottom segments. In the latter, more biofilms are formed.

Figure 3d shows the PC1 vs. PC2 scores plot of the *A.*-treated samples in the negative ion mode. The PC3 and PC4 scores and loadings plots are presented in Fig. S15. PC1, PC2, PC3, and PC4 explain 61.4%, 11.4 %, 7.6 % and 6.9% of all data in the *A.*-treated data set.

PC1 distinguishes the DI control seed and the *A.*-treated seed from *A.* bacteria controls. PC2 positive shows overlaps among the bottom of the DI control seed and the brush of the *A.*-treated seed. PC2 negative shows similarities among the top and bottom segments of the *A.*-treated and the *A.* biofilm. This result indicates that the top and bottom segments of *A.*-treated seed are more likely to be affected by the *A.* biofilm. Furthermore, the brush segment is more responsive to *A.* planktonic cells. Additional PCA results in the positive mode are shown in Figs. S16 and S17.

Flavonoids and phenolic acids

Flavonoids and phenolic acids have various functions as important secondary metabolites in plants, such as conferring antioxidant, anti-inflammatory, and biological antiviral activities.[38, 45, 46, 49] Thus, their metabolisms in the seed surface are of great interest. Figs. 3b-c and Figs. S14b-c show the selected peak spectral PCA loadings results of *P.*-treated samples, and Figs. 3e-f and Figs. S15b-c the selected peak spectral PCA loadings results of *A.*-treated samples in the negative ion mode, respectively.

Flavonoid (e.g., quercetin fragment m/z^- 121, $C_7H_5O_2^-$) and phenolic acids (e.g., cinnamic acid m/z^- 147, $C_9H_7O_2^-$) contribute to the PC1 negative loadings and PC2/PC4 positive loadings in the *P.*-treated samples; they also contribute to the PC1/PC3 negative loadings and PC4 positive loadings in the *A.*-treated samples. Combining with the scores plots, these compounds exist mostly in the top and brush sections of the *P.*-treated seed and in the brush segment of the *A.*-treated seed. P-hydroxybenzoic acid (m/z^- 137, $C_7H_5O_3^-$) and protocatechuic acid (m/z^- 153, $C_7H_5O_4^-$) contribute to the PC1 and PC2 positive loadings as well as the PC4 negative loadings in the *P.*-treated negative loadings. Looking into the scores plots, these compounds contribute mostly to the bottom and brush sections of the *P.*-treated seed; and to the top and bottom sections of the *A.*-treated seed. The p-hydroxybenzoic acid (m/z^- 137, $C_7H_5O_3^-$) is a plant metabolite and an algal metabolite.[66, 67] Protocatechuic acid (m/z^- 153, $C_7H_5O_4^-$) is a phenolic acid found in nature, and it is structurally similar to gallic acid, caffeic acid, vanillic acid, and syringic acid; and all are well-known antioxidant compounds.[68] Thus, the SIMS observations reasonably imply their functions in the plant-PGPR interactions.

The p-coumaric acid (m/z^- 163, $C_6H_{11}O_5^-$) and the galangin fragment (m/z^- 183, $C_{12}H_7O_2^-$) peaks are important contributors in the PC1 and PC2 negative loadings in the *P.*-treated samples. These compounds are also prominent in the PC1/PC2 negative loadings and PC3/PC4 positive loadings in the *A.*-treated samples. Referring to the scores plots, they contribute mostly in the brush section of the *P.*-treated seed and in the top to

bottom sections of the DI control seed and the *A.*-treated seed. p-Coumaric acid is a plant metabolite; and it has antioxidant and anti-inflammatory properties.[69] It is known to have bactericidal activity by destroying the bacterial cell membrane and interacting with bacterial DNA.[70] Galangin is a 7-hydroxyflavonol with additional hydroxy groups. It is an antimicrobial agent, and acts as an EC 3.1.1.3 (triacylglycerol lipase) inhibitor and a plant metabolite.[71] Gallic acid (m/z^- 169, $C_7H_5O_5^-$) is another important contributor in the PC1 negative loadings and PC2 positive loadings in the *P.*-treated samples. It contributes to the PC1, PC3 and PC4 negative loadings in the *A.* treated seed. The observation of phenolic acids and flavonoids indicates that important bacterial activities can be captured using ToF-SIMS.

To illustrate accumulations of flavonoids and phenolic acids in different PGPR-treated seeds, comparisons of normalized bar plots of these compounds are presented in Figs. S18 and S19. The comparison between the DI control seed and *P.*-treated seed is depicted in Fig. S18. The intensities of compounds such as p-hydroxybenzoic acid (m/z^- 137, $C_7H_5O_3^-$), cinnamic acid (m/z^- 147, $C_9H_7O_2^-$), and p–coumaric acid (m/z^- 163, $C_6H_{11}O_5^-$) are higher in the *P.*-treated seed than in the DI control seed in the top section. However, they decrease in the bottom segments. Two flavonoid peaks show an opposite trend. Specifically, the quercetin fragment (m/z^- 121, $C_7H_5O_2^-$) accumulates more in the DI control seed; while the galangin fragment (m/z^- 183, $C_{12}H_7O_2^-$) is more abundant in the *P.*-treated seed in both top and bottom sections. Fig. S19 presents a comparison between the DI control seed and *A.*-treated seed. Generally, the presence of phenolic acid is higher in the *A.*-treated seed than in the DI control seed. Gallic acid (m/z^- 169, $C_7H_5O_5^-$) is an exception among these peaks, because it shows an opposite trend. The galangin fragment (m/z^- 183, $C_{12}H_7O_2^-$) accumulates more than the quercetin fragment (m/z^- 121, $C_7H_5O_2^-$) in the PGPR treated seed, when comparing the PGPR treated seed and the DI control seed.

Previous studies report that flavonoids and phenolic acids have the anti-microbial function to protect plants from pathogens.[72] Our results show that these compounds exist in both the DI control seed and PGPR-treated seeds. Their appearances in the DI control seed may suggest a wounding response after the seed was sectioned. Additionally, their accumulations vary between different seed segments and PGPR treated seeds. For example, p-coumaric acid (m/z^- 163, $C_6H_{11}O_5^-$) is seemingly more sensitive to *A.* interactions. In contrast, quercetin and galangin have an opposite trend under different PGPR interactions, indicating different responses to PGPR. Optimizing the instrument setup and increasing the signal intensity will allow more unambiguous identification of metabolite related peaks. Utilizing the MS-MS capability in newer ToF-SIMS would certainly improve our abilities in peak identification.

Fatty acids

Fatty acids are vital components in bacterial biofilms and they also serve as structural membrane lipids in plants.[31, 51, 73] Many fatty acids, such as palmitic acid (m/z^- 255, $C_{16}H_{31}O_2^-$), margaric

acid (m/z^- 265, $C_{17}H_{29}O_2^-$), stearic acid (m/z^- 283, $C_{18}H_{35}O_2^-$), docosanoic acid (m/z^- 339, $C_{22}H_{43}O_2^-$) and cerotic acid (m/z^- 395, $C_{26}H_{51}O_2^-$), are significant contributors to the PC1 and PC4 negative loadings as well as the PC2 positive loadings in the *P.*-treated samples. They are prominent in the PC1 and PC4 negative loadings as well as PC2 positive loadings in the *A.*-treated samples. Thus, these fatty acids are important contributors in the *A.*- and *P.*-treated seeds combining the scores and loadings results.

Palmitic acid (m/z^- 255, $C_{16}H_{31}O_2^-$) and stearic acid (m/z^- 283, $C_{18}H_{35}O_2^-$) have higher loadings among the observed fatty acids. Palmitic acid (m/z^+ 257, $C_{16}H_{33}O_2^+$), and stearic acid (m/z^+ 285, $C_{18}H_{37}O_2^+$) have high loadings in the selected peak spectral PCA results in the positive mode (Figs. S16 and S17). This is expected since C16 and C18 fatty acids with three double bonds are the most abundant and common fatty acid constituents in membrane lipids of higher plants.[51, 74] Interestingly, palmitic acid serves as an important biomarker for biofilm functions in addition to being one of significant components in plant membranes.[34, 36, 75] Palmitic acid has high loadings in all samples, which might come from contributions from both the plant host and the bacteria. Biosynthesis of palmitic acid was reported in fungal and plant signaling.[76] In addition, fatty acids have antifungal and bactericidal functions;[77] and palmitic acid has stronger antifungal activity than unsaturated fatty acids.[78] Our data seems to support this finding.

Oleic acid (m/z^- 281, $C_{18}H_{33}O_2^-$) is prominent in the PC1, PC3, and PC4 negative loadings as well as PC2 positive loadings in the *A.*-treated samples. Antimicrobial lipids, including fatty acids and monoglycerides, can destabilize bacterial cell membranes and cause direct and indirect inhibitory effects. Our results support the notion that unsaturated oleic acid (C18:1) has a high potency in antibacterial activities in Gram-positive bacteria.[77, 79, 80] Arachidic acid (m/z^- 311, $C_{20}H_{39}O_2^-$) is another prominent contributor in the loadings of the two PGPR-treated samples. It was reported that arachidic acid (m/z^- 311, $C_{20}H_{39}O_2^-$) triggers fatty acid-mediated defense responses and elicits general plant stress-signaling networks.[81] Our results indicate that arachidic acid might participate in defense response when plants experience invading PGPR bacteria.

Quorum sensing inhibitor in plant response to PGPR exposure

In addition to auxin's role in plant growth, IAA has the ability to act as a quorum sensing inhibitor (QSI) of antivirulence by inhibiting antibiotic-resistant pathogens.[82-84] Bacteria can secrete chemical signal molecules and autoinducers to regulate cell density and a variety of physiological functions, such as bioluminescence and biofilm formation.[85] In this way, bacteria adapt to changes in the surrounding environment. This cell-to-cell communication behavior is called bacterial quorum sensing (QS).[86] Both Gram-positive and Gram-negative bacteria use QS and the mechnisms of their elicited responses from host organisms are different.[87, 88] QS can lead to the occurrence of pathogenicity in many plant pathogenic bacteria because bacterial behavior within biofilms is regulated by QS. Therefore, bacteria release chemical signals and express virulence factors.[89] For example, QS is responsible for enhanced

antibiotic tolerance of biofilms as well as for resistance to the innate immune system in *Pseudomonas aeruginosa*.[90] Therefore, the use of QSI has been proposed as a potential antivirulence approach.[91, 92]

IAA contributes to the PC1 negative loadings and PC2 positive loadings, in the positive spectral PCA results of *P.*-treated samples shown in Fig. S16, corresponding to the top segment of the *P.*-treated seed. *Pseudomonas fluorescens* are known for their plant growth-promoting properties including

pathogen suppression.[93] Our result indicates that IAA might play a QSI role in this process. Moreover, the IAA peak contributes notably in the PC1 and PC2 negative loadings coupled with PC1 and PC2 scores plots in the *A.*-treated PCA results in the positive ion mode (Fig. S17), which corresponds to the brush segment of the *A.*-treated seed. Consequently, our finding provides the molecular evidence for phytohormone IAA biosynthesis in the Gram-positive PGPR, which is consistent with a previous study of the IAA function in *Arthrobacter*.[94]
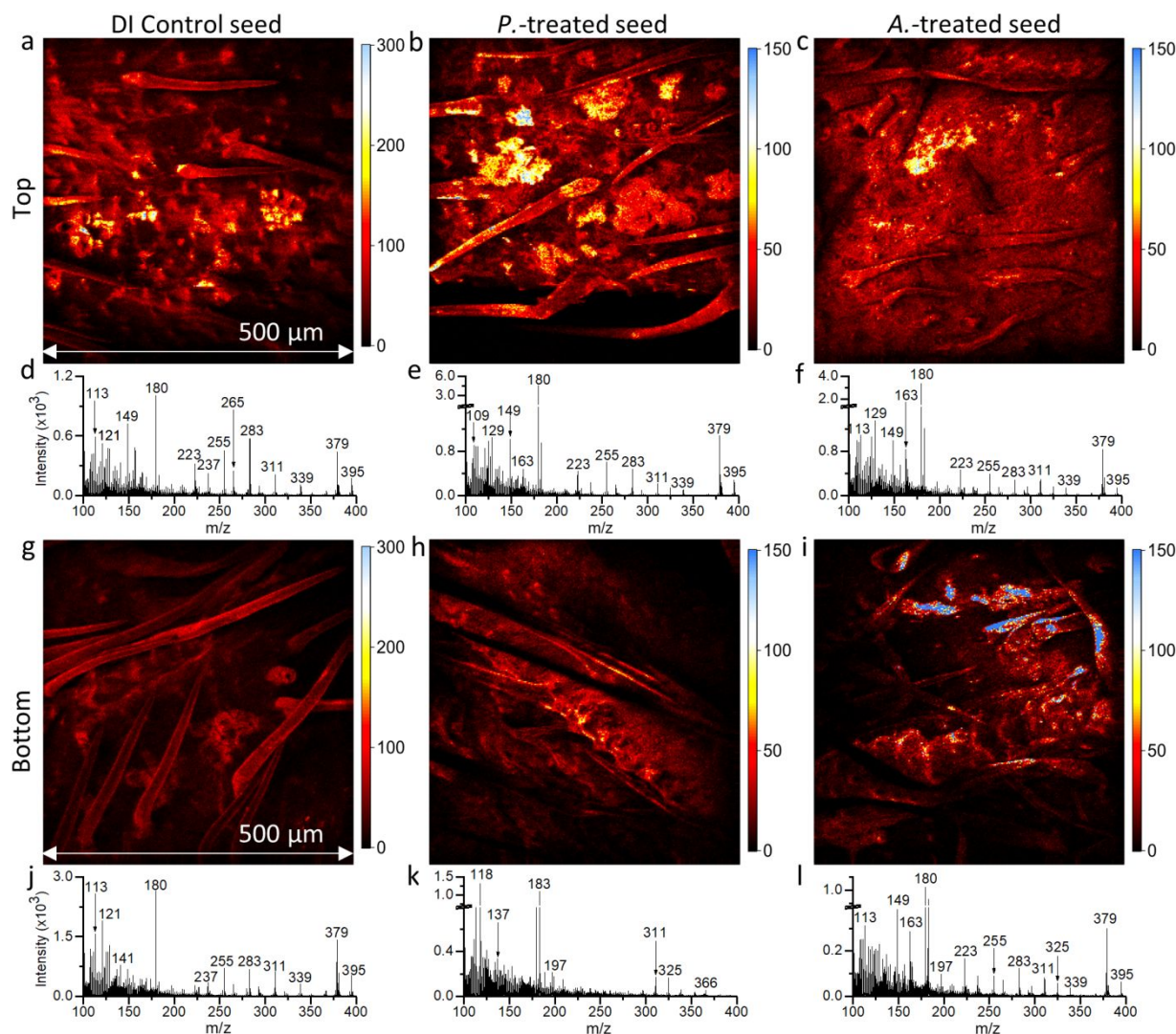
Fig. 4 Delayed extraction 2D total ion images of (a) DI control, (b) P.-treated and (c) A.-treated Brachypodium seed top sections and their corresponding spectra (d-f). Similarly, delayed extraction 2D total ion images of (g) DI control, (h) P.-treated, and (i) A.-treated Brachypodium seed bottom sections and their corresponding spectra (j-l) in m/z– $100 - 400$ in the negative ion mode.

Delayed extraction 2D images and spectra illustrate PGPR effects on the host seed surface

We have employed delayed extraction imaging in ToF-SIMS for the first time in the molecular mapping of plant-PGPR interactions. Figs. 4a-c and Figs. 4g-i depict the 2D total ions images in the top and bottom segments among treated seeds in the negative mode. The light blue color represents higher relative ion counts while darker color indicates lower counts. Clear distinctions are visualized at the surfaces of seeds that

have undergone different treatments. First, the appearance of the seed surfaces varies between the top and bottom sections of the same seed. Fiber-like hairs on the surface are shorter in the top segment compared to the bottom segment in the DI control seed. No fibers or hair structures are seen in the bottom segment in the *P.*-treated seed. Elongated fibers are barely seen while bumps have higher ion counts in the *A.*-treated seed. Second, the seed surfaces have obvious difference in the DI control seed and the PGPR-treated seeds when comparing the same seed sections. Fiber like structures on the *P.*-treated seed

are longer and thicker compared to the DI control seed in the top sections of seeds. In contrast, these fiber structures seem shriveled and small in the *A.*-treated seed surface. There are long black lines on the surface of the *P.*-treated seed compared to the DI control seed in the bottom sections. The surface of *A.*-treated seed does not have a lot of signals coming from these fiber-like structures. These 2D images show that ToF-SIMS not only captures morphologic features but also illustrate molecular changes using the delayed image extraction mode.

Figs. 4d-f and Figs. 4j-l demonstrate the delayed extraction spectral results of each samples in the range of m/z^- $100 - 400$ in the negative mode. The delayed extraction mode presents similar trends in the top section of the DI control and PGPR-treated seeds compared to spectral results from the static spectral mode shown in Fig. 2. For example, fatty acids such as myristic acid (m/z^- 222.98, $C_{14}H_{23}O_2^-$), palmitic acid (m/z^- 255.13, $C_{16}H_{31}O_2^-$), stearic acid (m/z^- 283.29, $C_{18}H_{35}O_2^-$), and arachidic acid (m/z^- 311.32, $C_{20}H_{39}O_2^-$) as well as the fragment of quercetin[1, 2B]$^-$ (m/z^- 120.99, $C_7H_5O_2^-$) are prominent. The delayed extraction mode spectral results show notable differences in the DI control and PGPR-treated seeds especially in the range of m/z^- $200 - 400$ in the bottom section. Only a few prominent peaks are seen in the *P.*-treated seed such as arachidic acid (m/z^- 311.32, $C_{20}H_{39}O_2^-$) and heneicosanoic acid (m/z^- 325.11, $C_{21}H_{41}O_2^-$). The low total ion intensities in the *P.*-treated seed likely contributes to the difficulty in observing higher mass ions. However, plant metabolites are still visible in the DI control seed and *A.*-treated seed in the delayed extraction mode spectral results. Figs. S20-S25 show the 2D image comparison of total ions and selected ions observed in the top and bottom seed sections in the SIMS negative ion mode. The representative metabolite flavonoid and fatty acid peaks are detected in the delayed extraction image mode. Although the total ion intensities in the bottom of *P.*-treated seed is relatively low, peaks such as palmitic acid (m/z^- 255.13, $C_{16}H_{31}O_2^-$) and stearic acid (m/z^- 283.29, $C_{18}H_{35}O_2^-$) are captured. In contrast, their signals are not significant in the high mass resolution spectral result. Additionally, a C4 plant Seteria leaf was used as a plant model to compare the images acquired from the high lateral resolution imaging mode and the delayed extraction mode in Figs. S26-S27, respectively. The 2D images acquired from the imaging mode (Fig. S26) provide a higher image resolution as expected with a trade-off in the loss of mass resolution. As a comparison, the delayed image results are useful in offering both reasonable morphological features (Fig. S27) and spectral information.

Overall, the spectra results from the delayed extraction mode (Figs. 4d-f and Figs. 4j-l) are consistent with the static high mass spectral observations (Fig 2). We discussed the functions of these metabolites on the host seed surface in the static spectral analysis and spectral PCA discussions. The delayed extraction mode 2D image and spectral results further assist the understanding of their roles in plant growth by inducing plant antimicrobial response to bacteria stress. The positive mode 2D and spectral analysis results (Figs. S28-S29) show similar observations. Both sets of imaging results support that the delayed image extraction mode could provide reasonable

findings compared to those acquired in the spectral mode. The delayed image extraction mode is useful to obtain plant morphological information while maintaining reasonable spectral fidelity in ToF-SIMS

Conclusions

We have applied ToF-SIMS, including the spectral mode and delayed image extraction mode, to characterize molecular and morphological changes in PGPR-affected Brachypodium seed surfaces for the first time. Vital plant metabolites and biomarkers are likely observed from the ToF-SIMS mass spectral analysis. Flavonoids and phenolic acids inherent in the host plants are found in the DI control and PGPR-treated seeds in SIMS spectral result and spectral PCA analyses. Our findings show that plants respond to microbial invasion by production of specific metabolites such as fatty acids. A common auxin, IAA, is observed in the PGPR-treated seed surfaces. In addition to its well-known function in promoting plant growth, our result suggests that IAA act as a QSI in the pathogen-suppression process of Gram-negative *P.* and Gram-positive *A.* The ion images from the delayed extraction mode provide visualization of morphological changes on the seed surface of PGPR-treated seeds, complemented with useful spectral information. Although ToF-SIMS has some limitations, such as its high cost and difficulty in operation and peak assignment, it is still a valuable and less explored tool in plant biology and microbiology. Our results in this paper show that ToF-SIMS has a great potential in capturing plant metabolites and tracking the bacteria – host relationship, and both are valuable in plant biology and systems biology. Moreover, ToF-SIMS can provide more insights into the cell-to-cell interactions offering submicrometer spatial resolution and molecular information.

Conflicts of interest

There are no conflicts to declare.

Acknowledgements

References

1. C. Jansson, J. Vogel, S. Hazen, T. Brutnell and T. Mockler, *J. Exp. Bot.*, 2018, **69**, 3801-3809.
2. A. H. Ahkami, R. Allen White, P. P. Handakumbura and C. Jansson, *Rhizosphere*, 2017, **3**, 233-243.
3. G. Berg, *Appl. Microbiol. Biotechnol.*, 2009, **84**, 11-18.
4. M. Choudhary and V. Nehra, *J. Appl. Nat. Sci.*, 2015, **7**, 540-556.
5. B. R. Glick, *Scientifica*, 2012, **2012**, 963401.
6. M. Ahemad and M. Kibret, *J. King Saud Univ. Sci.*, 2014, **26**, 1-20.
7. S. Compant, C. Clément and A. Sessitsch, *Soil Biol. Biochem.*, 2010, **42**, 669-678.
8. B. A. Boughton, D. Thinagaran, D. Sarabia, A. Bacic and U. Roessner, *Phytochem. Rev.*, 2016, **15**, 445-488.
9. L. W. Sumner, Z. Lei, B. J. Nikolau and K. Saito, *Nat. Prod. Rep.*, 2015, **32**, 212-229.
10. E. R. Amstalden van Hove, D. F. Smith and R. M. Heeren, *J. Chromatogr. A*, 2010, **1217**, 3946-3954.
11. R. G. Hemalatha and T. Pradeep, *J. Agric. Food Chem.*, 2013, **61**, 7477-7487.
12. M. Burrell, C. Earnshaw and M. Clench, *J. Exp. Bot.*, 2007, **58**, 757-763.
13. D. S. Dalisay, K. W. Kim, C. Lee, H. Yang, O. Rubel, B. P. Bowen, L. B. Davin and N. G. Lewis, *J. Nat. Prod.*, 2015, **78**, 1231-1242.
14. S. Yoon and T. G. Lee, *Nano Converg.*, 2018, **5**, 24.
15. T. Stephan, *Planet. Space Sci.*, 2001, **49**, 859-906.
16. J. C. Vickerman, *Analyst*, 2011, **136**, 2199-2217.
17. A. Seyer, J. Einhorn, A. Brunelle and O. Laprevote, *Anal. Chem.*, 2010, **82**, 2326-2333.
18. S. G. Boxer, M. L. Kraft and P. K. Weber, *Annu. Rev. Biophys.*, 2009, **38**, 53-74.
19. S. Fearn, *Mater. Sci. Technol.*, 2014, **31**, 148-161.
20. W. Liu, L. Huang, R. Komorek, P. P. Handakumbura, Y. Zhou, D. Hu, M. H. Engelhard, H. Jiang, X. Y. Yu, C. Jansson and Z. Zhu, *Analyst*, 2020, **145**, 393-401.
21. E. Gemperline, C. Keller and L. Li, *Anal. Chem.*, 2016, **88**, 3422-3434.
22. R. Tombolini, A. Unge, M. E. Davey, F. J. deBruijn and J. K. Jansson, *FEMS Microbiol. Ecol.*, 1997, **22**, 17-28.
23. K. Westerberg, A. M. Elvang, E. Stackebrandt and J. K. Jansson, *Int. J. Syst. Evol. Microbiol.*, 2000, **50 Pt 6**, 2083-2092.
24. L. L. Haney and D. E. Riederer, *Anal. Chim. Acta*, 1999, **397**, 225-233.
25. H. K. Shon, S. Yoon, J. H. Moon and T. G. Lee, *Biointerphases*, 2016, **11**, 02A321.
26. Q. P. Vanbellingen, N. Elie, M. J. Eller, S. Della-Negra, D. Touboul and A. Brunelle, *Rapid Commun. Mass Spectrom.*, 2015, **29**, 1187-1195.
27. F. Benabdellah, A. Seyer, L. Quinton, D. Touboul, A. Brunelle and O. Laprevote, *Anal. Bioanal. Chem.*, 2010, **396**, 151-162.
28. A. Henss, S. K. Otto, K. Schaepe, L. Pauksch, K. S. Lips and M. Rohnke, *Biointerphases*, 2018, **13**, 03B410.
29. J. L. S. Lee, I. S. Gilmore, I. W. Fletcher and M. P. Seah, *ApSS*, 2008, **255**, 1560-1563.
30. X. Hua, X. Y. Yu, Z. Wang, L. Yang, B. Liu, Z. Zhu, A. E. Tucker, W. B. Chrisler, E. A. Hill, T. Thevuthasan, Y. Lin, S. Liu and M. J. Marshall, *Analyst*, 2014, **139**, 1609-1613.
31. Y. Ding, Y. Zhou, J. Yao, C. Szymanski, J. Fredrickson, L. Shi, B. Cao, Z. Zhu and X. Y. Yu, *Anal. Chem.*, 2016, **88**, 11244-11252.
32. Y. Ding, Y. Zhou, J. Yao, Y. Xiong, Z. Zhu and X. Y. Yu, *Analyst*, 2019, **144**, 2498-2503.
33. R. Komorek, W. Wei, X. Yu, E. Hill, J. Yao, Z. Zhu and X. Y. Yu, *J. Vis. Exp*, 2017, DOI: 10.3791/55944.
34. W. Wei, Y. Zhang, R. Komorek, A. Plymale, R. Yu, B. Wang, Z. Zhu, F. Liu and X. Y. Yu, *Biointerphases*, 2017, **12**, 05G601.
35. W. Li, H. Li, J. Li, X. Cheng, Z. Zhang, F. Chai, H. Zhang, T. Yang, P. Duan, D. Lu and Y. Chen, *J. Environ. Sci.*, 2018, **69**, 61-76.
36. T. Leefmann, C. Heim, A. Kryvenda, S. Siljeström, P. Sjövall and V. Thiel, *Org. Geochem.*, 2013, **57**, 23-33.
37. F. Cuyckens and M. Claeys, *J. Mass Spectrom.*, 2004, **39**, 1-15.
38. P. Ristivojević, I. Dimkić, E. Guzelmeric, J. Trifković, M. Knežević, T. Berić, E. Yesilada, D. Milojković-Opsenica and S. Stanković, *LWT-Food Sci. Technol.*, 2018, **95**, 367-379.
39. Z. Benayad, C. Gomez-Cordoves and N. E. Es-Safi, *Int. J. Mol. Sci.*, 2014, **15**, 20668-20685.
40. H. J. Chen, B. S. Inbaraj and B. H. Chen, *Int. J. Mol. Sci.*, 2012, **13**, 260-285.
41. R. Shakya and D. A. Navarre, *J. Agric. Food Chem.*, 2006, **54**, 5253-5260.
42. D. J. Graham, M. S. Wagner and D. G. Castner, *ApSS*, 2006, **252**, 6860-6868.
43. X. Sui, Y. Zhou, F. Zhang, Y. Zhang, J. Chen, Z. Zhu and X.-Y. Yu, *Surf. Interface Anal.*, 2018, **50**, 927-938.
44. J. Son, Y. Shen, J. Yao, D. Paynter and X. Y. Yu, *Chemosphere*, 2019, **236**, 124345.
45. A. Y. Chen and Y. C. Chen, *Food Chem.*, 2013, **138**, 2099-2107.
46. Y. Li, J. Yao, C. Han, J. Yang, M. T. Chaudhry, S. Wang, H. Liu and Y. Yin, *Nutrients*, 2016, **8**, 167.
47. A. Wojdylo, J. Oszmianski and R. Czemerys, *Food Chem.*, 2007, **105**, 940-949.
48. M. Stobiecki, *Phytochemistry*, 2000, **54**, 237-256.
49. M. J. Simirgiotis, C. Quispe, J. Bórquez, G. Schmeda-Hirschmann, M. Avendaño, B. Sepúlveda and P. Winterhalter, *Ind. Crop. Prod.*, 2016, **85**, 159-166.
50. M. J. Taylor, K. Y. Zhang, D. J. Graham and L. J. Gamble, *Surf. Sci. Spectra*, 2018, **25**.
51. A. A. Millar, M. A. Smith and L. Kunst, *Trends Plant Sci.*, 2000, **5**, 95-101.
52. E. B. Monroe, J. C. Jurchen, J. Lee, S. S. Rubakhin and J. V. Sweedler, *J. Am. Chem. Soc.*, 2005, **127**, 12152-12153.
53. T. Leefmann, C. Heim, S. Siljestrom, M. Blumenberg, P. Sjovall and V. Thiel, *Rapid Commun. Mass Spectrom.*, 2013, **27**, 565-581.
54. S. Munne-Bosch, *J. Plant Physiol.*, 2005, **162**, 743-748.
55. J. Nordberg and E. S. Arner, *Free Radical Bio. Med.*, 2001, **31**, 1287-1312.
56. O. A. Palacios, Y. Bashan and L. E. de-Bashan, *Biol. Fertility Soils*, 2014, **50**, 415-432.
57. M. S. Greenwood, S. Shaw, J. R. Hillman, A. Ritchie and M. B. Wilkins, *Planta*, 1972, **108**, 179-183.
58. S. Spaepen and J. Vanderleyden, *CSH Perspect. Biol.*, 2011, **3**.
59. D. Duca, J. Lorv, C. L. Patten, D. Rose and B. R. Glick, *Anton. Leeuw. Int. J. G.*, 2014, **106**, 85-125.
60. E. Khare and N. K. Arora, *Curr. Microbiol.*, 2010, **61**, 64-68.
61. D. K. Malik and S. S. Sindhu, *Physiol. Mol. Biol. Plants*, 2011, **17**, 25-32.
62. S. Tabatabaei, P. Ehsanzadeh, H. Etesami, H. A. Alikhani and B. R. Glick, *Span. J. Agric. Res.*, 2016, **14**.
63. M. Ozdal, O. G. Ozdal, A. Sezen, O. F. Algur and E. B. Kurbanoglu, *3 Biotech*, 2017, **7**, 23.
64. C. Forni, J. Riov, M. Grilli Caiola and E. Tel-Or, *J. Gen. Microbiol.*, 1992, **138**, 377-381.
65. C. Yang, W. Wei, F. Liu and X. Y. Yu, *Biointerphases*, 2019, **14**, 051004.

66. C. Zidorn, *Phytochemistry*, 2016, **124**, 5-28.

67. L. Onofrejova, J. Vasickova, B. Klejdus, P. Stratil, L. Misurcova, S. Kracmar, J. Kopecky and J. Vacek, *J. Pharm. Biomed. Anal.*, 2010, **51**, 464-470.

68. S. Kakkar and S. Bais, *ISRN Pharmacol*, 2014, **2014**, 952943.

69. S. J. Pragasam, V. Venkatesan and M. Rasool, *Inflammation*, 2013, **36**, 169-176.

70. Z. Lou, H. Wang, S. Rao, J. Sun, C. Ma and J. Li, *Food Control*, 2012, **25**, 550-554.

71. N. A. Lunagariya, N. K. Patel, S. C. Jagtap and K. K. Bhutani, *EXCLI J*, 2014, **13**, 897-921.

72. L. S. Chua, N. A. Latiff, S. Y. Lee, C. T. Lee, M. R. Sarmidi and R. A. Aziz, *Food Chem.*, 2011, **127**, 1186-1192.

73. Y. Li, Y. H. Li, P. Yang, H. A. Zhang and D. He, *Hortic. Environ. Biotechnol.*, 2017, **58**, 334-341.

74. T. Yaeno, O. Matsuda and K. Iba, *Plant J.*, 2004, **40**, 931-941.

75. Y. K. Magnusson, P. Friberg, P. Sjovall, J. Malm and Y. Chen, *Obesity*, 2008, **16**, 2745-2753.

76. M. Trepanier, G. Becard, P. Moutoglis, C. Willemot, S. Gagne, T. J. Avis and J. A. Rioux, *Appl. Environ. Microbiol.*, 2005, **71**, 5341-5347.

77. J. J. Kabara, D. M. Swieczkowski, A. J. Conley and J. P. Truant, *Antimicrob. Agents Chemother.*, 1972, **2**, 23-28.

78. S. Liu, W. Ruan, J. Li, H. Xu, J. Wang, Y. Gao and J. Wang, *Mycopathologia*, 2008, **166**, 93-102.

79. B. K. Yoon, J. A. Jackman, E. R. Valle-Gonzalez and N. J. Cho, *Int. J. Mol. Sci.*, 2018, **19**.

80. S. E. Walsh, J. Y. Maillard, A. D. Russell, C. E. Catrenich, D. L. Charbonneau and R. G. Bartolo, *J. Appl. Microbiol.*, 2003, **94**, 240-247.

81. T. Savchenko, J. W. Walley, E. W. Chehab, Y. Xiao, R. Kaspi, M. F. Pye, M. E. Mohamed, C. M. Lazarus, R. M. Bostock and K. Dehesh, *Plant Cell*, 2010, **22**, 3193-3205.

82. W. Chu, T. R. Zere, M. M. Weber, T. K. Wood, M. Whiteley, B. Hidalgo-Romano, E. Valenzuela, Jr. and R. J. McLean, *Appl. Environ. Microbiol.*, 2012, **78**, 411-419.

83. Q. H. Christensen, T. L. Grove, S. J. Booker and E. P. Greenberg, *Proc. Natl. Acad. Sci. USA*, 2013, **110**, 13815-13820.

84. J. H. Lee, T. K. Wood and J. Lee, *Trends Microbiol.*, 2015, **23**, 707-718.

85. A. Kumari, P. Pasini, S. K. Deo, D. Flomenhoft, H. Shashidhar and S. Daunert, *Anal. Chem.*, 2006, **78**, 7603-7609.

86. W. C. Fuqua, S. C. Winans and E. P. Greenberg, *J. Bacteriol.*, 1994, **176**, 269-275.

87. B. L. Bassler, *Curr. Opin. Microbiol.*, 1999, **2**, 582-587.

88. M. B. Miller and B. L. Bassler, *Annu. Rev. Microbiol.*, 2001, **55**, 165-199.

89. V. C. Kalia, *Biotechnol. Adv.*, 2013, **31**, 224-245.

90. T. B. Rasmussen and M. Givskov, *Int. J. Med. Microbiol.*, 2006, **296**, 149-161.

91. M. Hentzer, H. Wu, J. B. Andersen, K. Riedel, T. B. Rasmussen, N. Bagge, N. Kumar, M. A. Schembri, Z. Song, P. Kristoffersen, M. Manefield, J. W. Costerton, S. Molin, L. Eberl, P. Steinberg, S. Kjelleberg, N. Hoiby and M. Givskov, *EMBO J.*, 2003, **22**, 3803-3815.

92. G. Brackman, P. Cos, L. Maes, H. J. Nelis and T. Coenye, *Antimicrob. Agents Chemother.*, 2011, **55**, 2655-2661.

93. P. Flury, N. Aellen, B. Ruffner, M. Pechy-Tarr, S. Fataar, Z. Metla, A. Dominguez-Ferreras, G. Bloemberg, J. Frey, A. Goesmann, J. M. Raaijmakers, B. Duffy, M. Hofte, J. Blom, T. H. Smits, C. Keel and M. Maurhofer, *ISME J.*, 2016, **10**, 2527-2542.

94. M. Li, R. Guo, F. Yu, X. Chen, H. Zhao, H. Li and J. Wu, *Int. J. Mol. Sci.*, 2018, **19**.